

Enhanced Electrochemical Performance by GeO_x-Coated MXene Nanosheet Anode in Lithium-ion Batteries

Chenguang Liu^{a,b}, Yinchao Zhao^{a,b}, Ruowei Yi^{c,d}, Hao Wu^a, Wenbin Yang^a, Yinqing Li^e, Ivona Mitrovic^b, Stephen Taylor^b, Paul Chalker^f, Rui Liu^g, Li Yang^{c*}, Cezhou Zhao^{a*}

^a*Department of Electrical and Electronic Engineering, Xi'an Jiaotong-Liverpool University, Suzhou 215123, China*

^b*Department of Electrical Engineering and Electronics, University of Liverpool, Liverpool L69 3GJ, UK*

^c*Department of Chemistry, Xi'an Jiaotong-Liverpool University, Suzhou, Jiangsu 215123, China*

^d*Stephenson Institute for Renewable Energy, Department of Chemistry, University of Liverpool, Liverpool L69 7ZD, UK*

^e*Dongguan Hongde Battery Ltd. Co., Dongguan 523649, China*

^f*Centre for Advanced Materials, University of Liverpool, L69 3GH, UK*

^g*National Demonstration Center for Experimental Materials Science and Engineering Education, Jiangsu University of Science and Technology, Zhenjiang, 212003, China*

*Corresponding authors.

E-mail addresses: cezhou.zhao@xjtlu.edu.cn (C. Zhao); li.yang@xjtlu.edu.cn (L. Yang)

Abstract

Here, we demonstrate a facile method to synthesize an amorphous GeO_x -coated MXene nanosheet structure as the anode in lithium-ion batteries. By using the GeO_3^{2-} as the precursor, NaBH_4 as the reduction agent, we performed a one-pot in situ synthesis to prepare a composite of GeO_x nanoparticles coated on MXene nanosheet. The size of the GeO_x nanoparticles is approximately 50 nm, which offers abundant contact surface between active materials with the electrolyte, as well as fast pathways for Li-ion interaction. Moreover, the unique two-dimensional MXene nanosheet serves as the excellent conductive additives to improve the electrochemical stability and electrical conductivity of composite when used in LIBs. The results indicate that the $\text{GeO}_x/\text{MXene}$ nanosheet structure significantly improves the stability during the lithiation/delithiation processes, with the enhanced capacity through an improved kinetic process. Another attractive element of this novel anode is the flexibility to tune the electrochemical properties by using different combination of binder and solvent when the slurry is prepared for the electrode fabrication. The electrode prepared with polyvinylidene fluoride binder and N-methyl pyrrolidinone solvent exhibits an excellent sustainable capacity of 381 mAh g^{-1} at 15 A g^{-1} . By contrast, the electrode with lithium polyacrylate and de-ionized water delivers a reversible capacity of 950 mAh g^{-1} at 0.5 A g^{-1} after 100 cycles. These interesting results are ascribed to the inner characteristic structure of the two types of electrodes, which have been verified by electrochemical kinetics and scanning electron microscopic images. It also reveals that the different dispersion state is responsible to the difference of electrochemical

properties, which highlights the importance of the electrode design for high-performance lithium-ion batteries.

Keywords: GeO_x anode; MXene nanosheet; Binder; Solvent; Lithium-ion batteries

Introduction

Since its discovery, lithium-ion batteries (LIBs) have the ability to deliver high energy density with long cycle lifetime on many applications such as wearable electronics, power devices, energy storage systems, hybrid electric vehicles (HEV), and electric vehicles (EV). [1-4] Many advanced developments of LIBs are being explored to meet the increasing demands. In recent years research efforts have significantly expanded the choices of anode materials other than the current commercial graphite, because the theoretical capacity of graphite (372 mAh g^{-1}) hardly satisfied the requirements of advanced high-performance LIBs [5]. The germanium oxide has been considered as a promising candidate for the novel anode materials, [6] taking advantage of the characteristic lithiation process of the germanium oxide [7]:



Equation (1) represents the irreversible reduction of germanium oxide in the first stage. Meanwhile, the generation of lithium oxide could hinder the aggregation and buffer the volume changes of the Ge nanoparticles. Equation (2) illustrates the reversible lithiation and delithiation processes of the Ge, contributing a theoretical capacity of 1100 mAh g^{-1} , about 3 times higher than that of the commercial graphite anode.

However, germanium oxide faces similar challenges with tin and silicon, suffering the tremendous volume expansion (370% for the full lithiation of Ge) and low conductivity during the discharge and charge of LIBs [8]. These problems cause the pulverization of the Ge-based anode and the formation of thicker solid electrolyte interface (SEI) on the

material surface, subsequently leading to the rapid capacity fading and the loss of interparticle electrical contact.

To date, various approaches have been reported to tackle these issues, consisting of mainly improved morphologies design (nanoparticles [9], nanowires [10], nanoribbons [11], nanotubes [12] and porous structures [13]), metal-doped germanium oxide [14-17], two-dimensional (2D) materials enhanced germanium oxide [18-20], GeO_x nanoparticle [21] and GeO_x-based composite [22, 23]. In particular, the GeO_x-based composite and 2D materials have demonstrated enormous potential in increasing the rate performance and cycling stability of LIBs. Wang and his research group initially synthesized the hierarchical porous GeO_x, using GeO₃²⁻ as the precursor, and NaBH₄ as the reducing agent. Outstanding cycling stability was demonstrated when the hierarchical porous GeO_x was used as the anode in LIBs. [21] Inspired by their work, Lv et al. demonstrated an approach to combine GeO_x with reduced graphene oxide (RGO), to improve electrical conductivity and rate performance of LIBs. [22] Following these studies, Choi et al. applied the polystyrene (PS) nanobeads as sacrificial templates and fabricated a sandwich structure of GeO_x coated on RGO balls for LIBs, with the hope to provide the short pathway for Li-ion diffusion, resulting in excellent long-term cycling performance with high reversible capacities. [23] These examples confirmed that the composite of GeO_x materials with 2D materials (here RGO for example) is a feasible pathway to achieve stable electrochemical properties and exceptional rate performance of LIBs.

Inspired by the introduction of 2D materials to the GeO_x anode, a novel member of 2D materials family, MXene combined highly electrical conductivity of graphene and outstanding hydrophilia of graphene oxide is worth exploring. [24, 25] Use of joint MXene and the GeO_x as the LIBs anode has not yet found in the literature. The MXene $\text{Ti}_3\text{C}_2\text{T}_x$ (T indexed to the terminal groups such as -OH, -O, and -F) could be facily achieved with the 2D layered structure by using LiF and HCl to exfoliate layered carbides with MAX phases [26, 27]. During the Li-ions interaction/de-interaction process, the MXene shows subtle volume change and low Li-ion diffusion barrier.[28, 29] It provides a stable mechanical capacity and convenient interaction channel to support the electrochemical stability when combined with other materials. Thus, the MXene has been used in many energy storage fields such as LIBs and supercapacitors [30-32].

Herein, we reported a facile method to fabricate a $\text{GeO}_x/\text{MXene}$ nanosheet as a LIBs anode by growing the thin film of GeO_x on the MXene sheets. This novel nanostructure not only provides a fast pathway for Li-ions interaction with superior electrical conductivity but also demonstrates a stable electrochemical performance due to the mechanical capacity of MXene. These excellent features result in good rate performance and stable reversible capacity during lithiation/delithiation cycles. Remarkably, the attractive feature of this $\text{GeO}_x/\text{MXene}$ nanosheet anode is to utilize flexible tuning of electrochemical properties when employed with different choices of solvent and binder. Two different types of the electrode were prepared. One is water-soluble lithium polyacrylate (Li-PAA) binder and de-ionized (DI)-water solvent,

another one is water-insoluble polyvinylidene fluoride (PVDF) binder and N-methyl pyrrolidinone (NMP) solvent. Two types of the electrode have demonstrated different electrochemical features, revealing the choice of solvent and binder could significantly influence the electrode properties in the LIBs.

Experiment Section

Synthesis of $Ti_3C_2T_x$

The MXene ($Ti_3C_2T_x$) was synthesized by etching precursor Ti_3AlC_2 ($< 32 \mu m$) with LiF/HCl as reported previously. [33] Typically, LiF (2 g, Aladdin) and HCl (40 ml, 9 M, Sinopharm Chemical Reagent) were mixed by stirring in a Teflon beaker. Then, Ti_3AlC_2 powder (1 g) was slowly added into the mixture of the acid solution for 24 h at 35 °C. After the reaction, the resultant was washed with several centrifugation-rinsing cycles (3500 rpm for 10 min) with de-ionized (DI)-water until the PH of the resultant solution is approaching to 6. Then, the washed resultant was dispersed in 40 ml of ethanol and kept under ultrasonic for 1.5 h. After this exfoliation process, the dark grey product was collected by centrifugation at 10000 rpm for 10 min. To get the finally dark green MXene supernatant, the dark grey product was re-dispersed in DI-water and kept under ultrasonic for 20 min, and then treated by 5 min centrifugation at 3500 rpm to separate the sediment.

Synthesis of MXene@GeO_x

Firstly, 0.03 g polyvinyl pyrrolidone (PVP) was dispersed into 25 mL of the MXene dispersion (12 mg/ml) by ultrasonication. Meanwhile, 500 mg GeO₂ was added to 5 ml DI-water at 70 °C and then followed by adding the 2.5 ml ammonia (13.2 mol L⁻¹) into the GeO₂ suspension. After that, the GeO₂/ammonia mixture was quickly transferred to a transparent and clear solution. After that, this mixture was added to PVP/MXene dispersion with further ultrasonic treatment. Then, the NaBH₄ (0.9 g NaBH₄ adding into 20 mL DI-water with ice-water bath) was added into the above mixture solution by drop

wise with magnetic stirring. After 12 h magnetic stirring, the dark-green suspension was obtained and then the resulting powder was collected by centrifugation and washed with ethanol several times. Finally, these collected powder was dried in the vacuum furnace at 60 °C overnight. The control sample of pure GeO_x was prepared by a similar approach, except for the addition of MXene nanosheet.

Structural characterization

The microstructure and morphologies of the achieved samples were examined under the high-resolution transmission electron microscopy (HR-TEM, FEI Tecnai G2 F30) and field-emission scanning electron microscopy (FE-SEM, Hitachi S-4800). The crystal structure of resultant materials was characterized by a Bruker Advance D8 (Cu Ka) X-ray powder diffraction meter (XRD) from 3 to 80 ° at 5 degrees· min⁻¹. The X-ray photoelectron spectroscopy (XPS) patterns were measured by Thermo scientific ESCALAB 250Xi with Al Ka X-ray source. The thermogravimetric (TG) curve was determined by the TA Instruments SDT2960 from room temperature to 1200 °C with a heating rate of 10 °C min⁻¹ under the argon atmosphere. The atomic force microscopy (AFM) images were acquired by the Bruker MultiMode 8.

Electrochemical measurements

The electrochemical performance of the GeO_x/MXene and GeO_x were performed by using coin cells with CR2032-type. For the investigation of different types of slurry, the achieved GeO_x/MXene samples were firstly mixed with the different binder (PVDF or Li-PAA) and conductive additive Super-P with a weight ratio of 8:1:1, while the NMP or DI-water was respectively used for PVDF and DI-water as the solvent. This slurry

was then coated on the copper foil followed by drying at 60 °C for 10 h. On average, the electrode mass loading was about 1.35 mg⁻². The electrodes with 13 mm diameter were punched from the dried slurry/copper foil. The lithium metal was used for the negative electrode. The coin cells were assembled in an argon-filled glove box (H₂O, O₂ < 0.2 ppm). Each cell was composed of a GeO_x/MXene electrode, Celgard 2325 separator, lithium metal negative electrode, and 1 M LiPF₆ in a solution mixture of dimethyl carbonate (DMC) and ethylene carbonate (EC) (1:1 vol%) electrolyte. The cycling voltammetry (CV) test with the scanning rate of 0.1 mV s⁻¹ was measured on a Metrohm Autolab PGSTAT302N electrochemical workstation. The electrochemical impedance spectroscopy (EIS) was also measured from 0.01 Hz to 1 MHz on Autolab PGSTAT302N electrochemical workstation. For the galvanostatic cycling test of batteries, the Neware BTS-4000 multichannel batteries test system was used with a cut-off voltage between 0.01 V and 1.2 V.

For simplicity, the electrode samples were labeled with different abbreviations according to the preparing approaches of slurry. GeO_x/MXene/PVDF (NMP) and GeO_x/PVDF (NMP) represent the GeO_x/MXene and pure GeO_x electrode with PVDF binder and NMP solvent. GeO_x/MXene/Li-PAA (DI-water) and GeO_x/Li-PAA (DI-water) represent the GeO_x/MXene and pure GeO_x electrode with Li-PAA binder and DI-water solvent.

Result and Discussion

GeO_x-Coated MXene Nanosheet Anode in LIBs

Fig. 1 shows the fabrication process of the GeO_x/MXene nanosheet composite. The GeO_x/MXene composite was prepared by a one-pot method that only involves one chemical reaction. As shown in the schematic diagram (Fig. 1), the subsequent mixing of MXene (Ti₃C₂T_x, Fig. S1 and S2) and PVP forms a PVP coating on the MXene nanosheet. Upon mixing, the hydrophilic head of PVP would interconnect with the surface of the MXene nanosheet. The hydrophobic tail acts as a template to assist the formation of small size GeO_x nano particles which will be anchored on MXene nanosheet. Meanwhile, the GeO₃²⁻ precursor prepared by the mixing of GeO₂ with ammonia is added into the MXene/PVP mixture and followed by reducing of Ge ions using NaBH₄. In this reaction, the PVP plays a role as a capping ligand to constrain the size of nanoparticles, allowing the GeO_x nanoparticles to be in-situ reduced from GeO₃²⁻ by NaBH₄

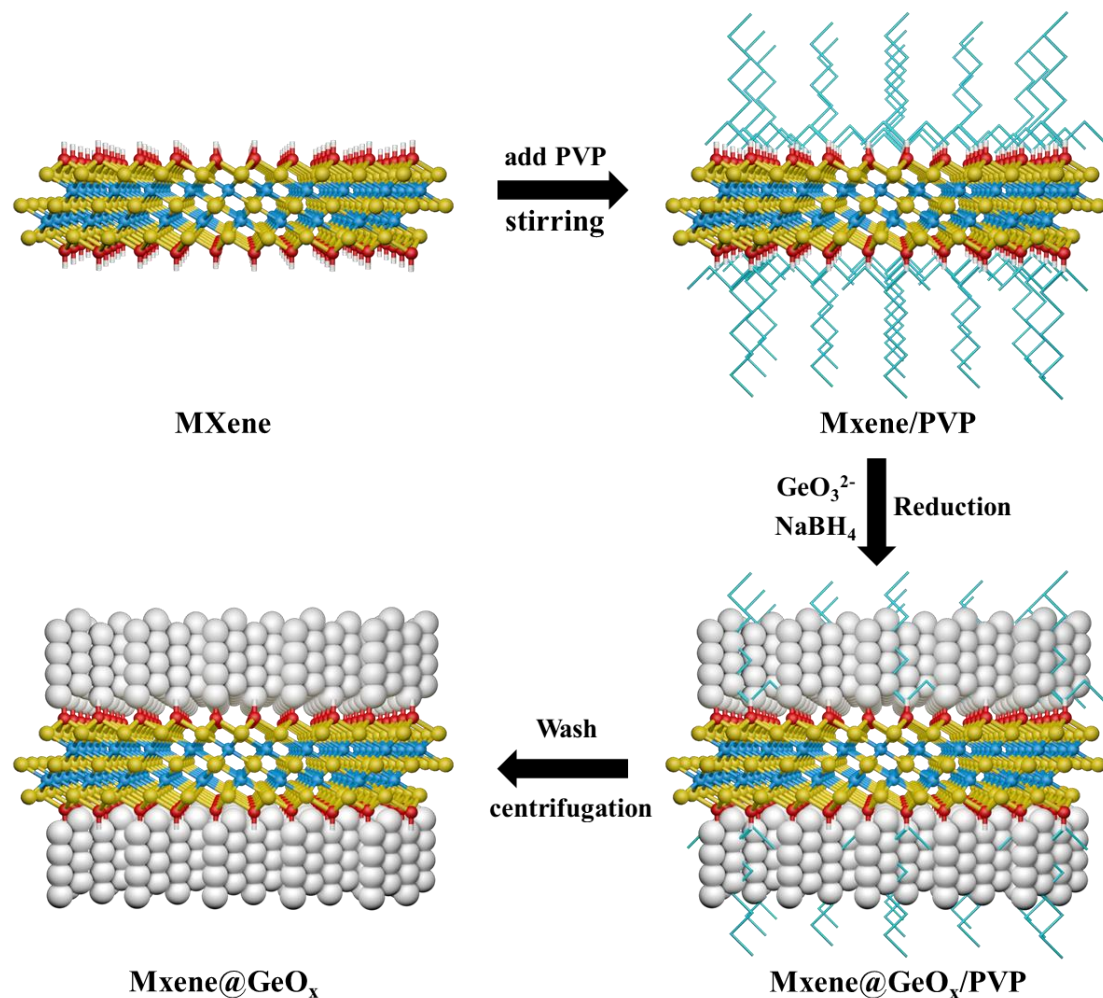


Fig. 1 The schematic diagram for the fabrication of the GeO_x/MXene nanosheet composite.

The morphologies and structure of the as-prepared sample were characterized as shown in Fig. 2. The SEM images (Fig. 2a and 2b) show the GeO_x/MXene nanosheets dispersing on the substrate. The GeO_x nanostructure is uniformly coated on the MXene, without unexpected agglomeration and damage of the MXene original sheet-like structure. To further determine the nanostructure of GeO_x, the GeO_x/MXene nanosheets were examined under the atomic force microscope (AFM) as shown in Fig. 2f. Clearly, the GeO_x nanoparticles are piled up on the MXene nanosheets. The diameter and

thickness of the GeO_x nanoparticles were measured around 50 nm and 20 nm respectively (Fig. S3). This indicates that the nanostructure of particles can significantly improve the contact surface between active materials with the electrolyte, as well as provide fast pathways for Li-ion insertion. The alternative composite structure was further confirmed by TEM in Fig. 2c-2d. Surprisingly, $\text{GeO}_x/\text{MXene}$ nanosheets appear slightly stacked and well distributed in the field of view. The high-resolution TEM image of $\text{GeO}_x/\text{MXene}$ (Fig. 2d) further illustrates the successful integration, in which amorphous GeO_x is intimately coated on the MXene film, with the distinct layered structure of the MXene sheets. The thickness of MXene nanosheet is around 2.14 nm by AFM, as shown in Fig. S2. This thickness was consistent with the result of the TEM image in Fig. 2b, and confirmed the existence of the monolayer MXene nanosheet in our sample. The EDS mapping of the as-obtained $\text{GeO}_x/\text{MXene}$ nanosheet (Fig 2e) also shows a uniform distribution of Ti, C, Ge, O on the composites, indicating the uniform growth of the GeO_x on the MXene sheets by the self-assembly processes and in-situ reduction. To validate the surface textures and nanostructure of the $\text{GeO}_x/\text{MXene}$ nanosheet, the pore size distribution, and nitrogen adsorption isotherms are displayed in Fig. 2g and Fig. S4. The specific surface area (SSA) of the MXene and $\text{GeO}_x/\text{MXene}$ nanosheet obtained by Brunauer–Emmett–Teller (BET) method is $41.47 \text{ m}^2 \text{ g}^{-1}$ and $124.88 \text{ m}^2 \text{ g}^{-1}$ respectively. The significant increment of the SSA in $\text{GeO}_x/\text{MXene}$ is attributed to the uniformity of coated GeO_x on the MXene. In Fig. 2g, the pore size distribution of $\text{GeO}_x/\text{MXene}$ is in a wide range from 1.8 to 50 nm, which is in a good agreement with AFM and TEM observation.

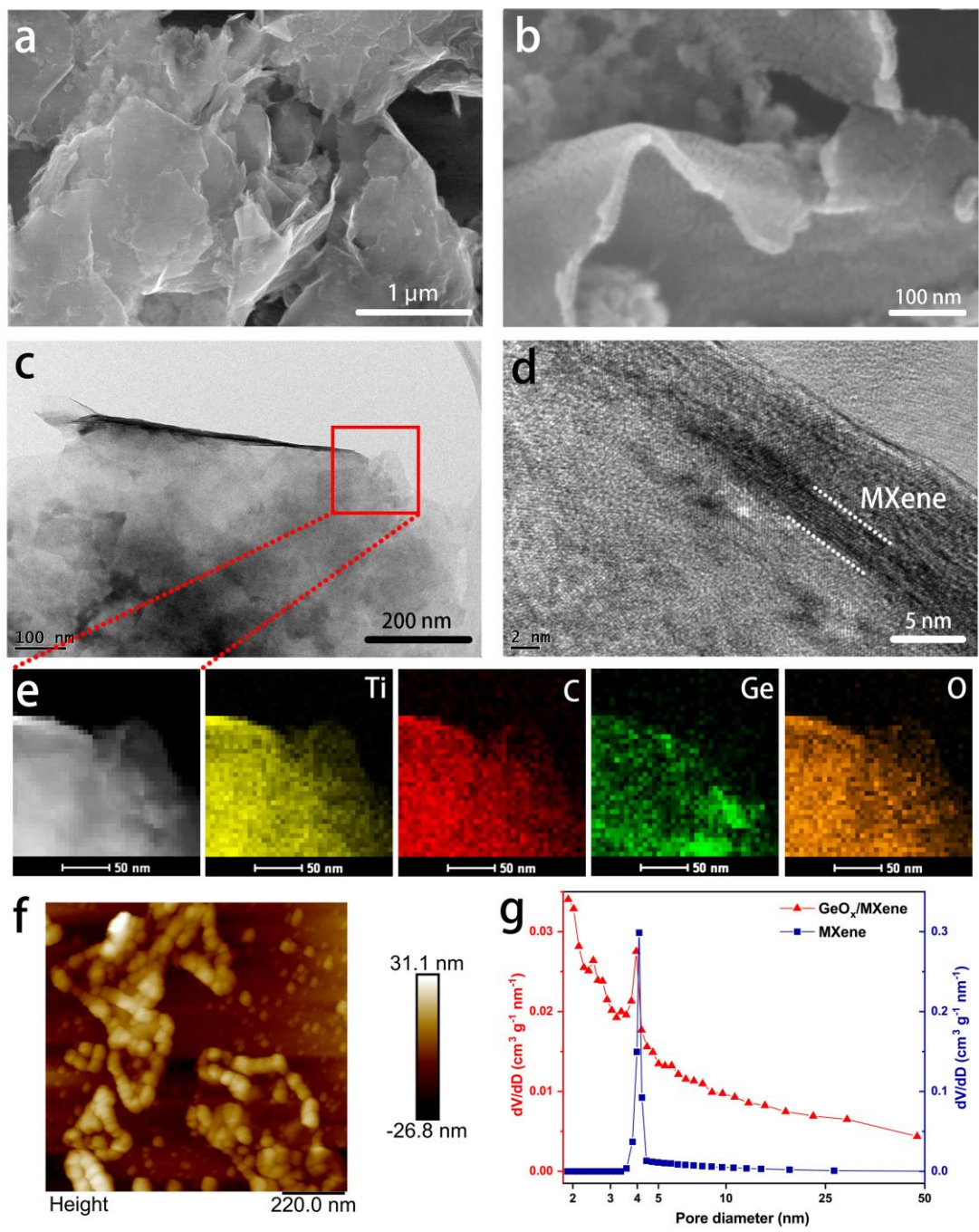


Fig. 2 (a and b) Field emission SEM images of the GeO_x/MXene nanosheet structure, (c) TEM image of the GeO_x/MXene nanosheet structure, (d) High-resolution TEM image showing the stacking of MXene; (e) EDS mapping images of Ti, C, Ge, and O elements for the marked red box shown in (c); (f) AFM image showing GeO_x nanoparticles piled up on the MXene sheets; (g) Pore size distribution obtained by the BET method.

The amorphous feature of GeO_x could be further confirmed by the XRD patterns (Fig. 3a). For the $\text{GeO}_x/\text{MXene}$ composite, there are only two sharp diffraction peaks locating at 4° and 60.1° , corresponding to the MXene (002) and (110). After a simple heat-treatment at 700°C under Ar for 2 hours, several new sharp diffraction peaks were observed in the pattern, which is explained by decomposing the GeO_x into Ge and GeO_2 at 700°C . These peaks are associated with crystalline planes of GeO_2 (101), (112), (113) (JCPDS #65-0862) and Ge (111), (220), (311), (400), (311) (JCPDS #65-0333), respectively. Since pure GeO_2 and Ge are the consequence of the heat-treatment, it indicates that the oxidation species of germanium in the composite is amorphous GeO_x (where x is smaller than 2). As further approved in Fig 3b-d, the XPS spectra of Ti $2p$, Ge $3d$, and O $1s$ for $\text{GeO}_x/\text{MXene}$ composite provides more information about the chemical environment of the composite. Fig 3b shows the Ti $2p$ spectrum of the $\text{GeO}_x/\text{MXene}$ composite, in which, the Ti-C, Ti^{2+} , and Ti^{3+} peaks are consistent with the previous report.[25] It demonstrates that the growth process of GeO_x is mild and the MXene structure remains intact after the GeO_x growth. From Ge $3d$ spectrum (Fig 3c), there are 4 peaks located at 29.3, 31.1, 32.0, and 32.6 eV after the deconvoluted fitting, corresponding to Ge^0 , Ge^{2+} , Ge^{3+} , and Ge^{4+} , respectively.[23] The peak centered at 29.4 eV confirms the existence of Ge^0 in the particles. The main peak at 32.5 eV is fitted to three peaks at 31.1, 32.0, and 32.6 eV corresponding to Ge^{2+} , Ge^{3+} , and Ge^{4+} . The peak area calculation of this Ge $3d$ spectrum indicates that the surface of GeO_x consists of Ge^0 (6.02 %), Ge^{2+} (3.98 %), Ge^{3+} (36.77 %), and Ge^{4+} (53.21 %). The G:O stoichiometry ratio of 1:1.65 is determined by the Ge $3d$ spectrum, which confirms the

moderate oxidation of GeO_x . Moreover, the XPS spectrum of O 1s (Fig. 3d) implies the composition of GeO_x with MXene. The Ti-O, Ti-C-O_x, Ti-C-OH, Ge-O, and absorbed H₂O are also identified in the O 1s spectrum.

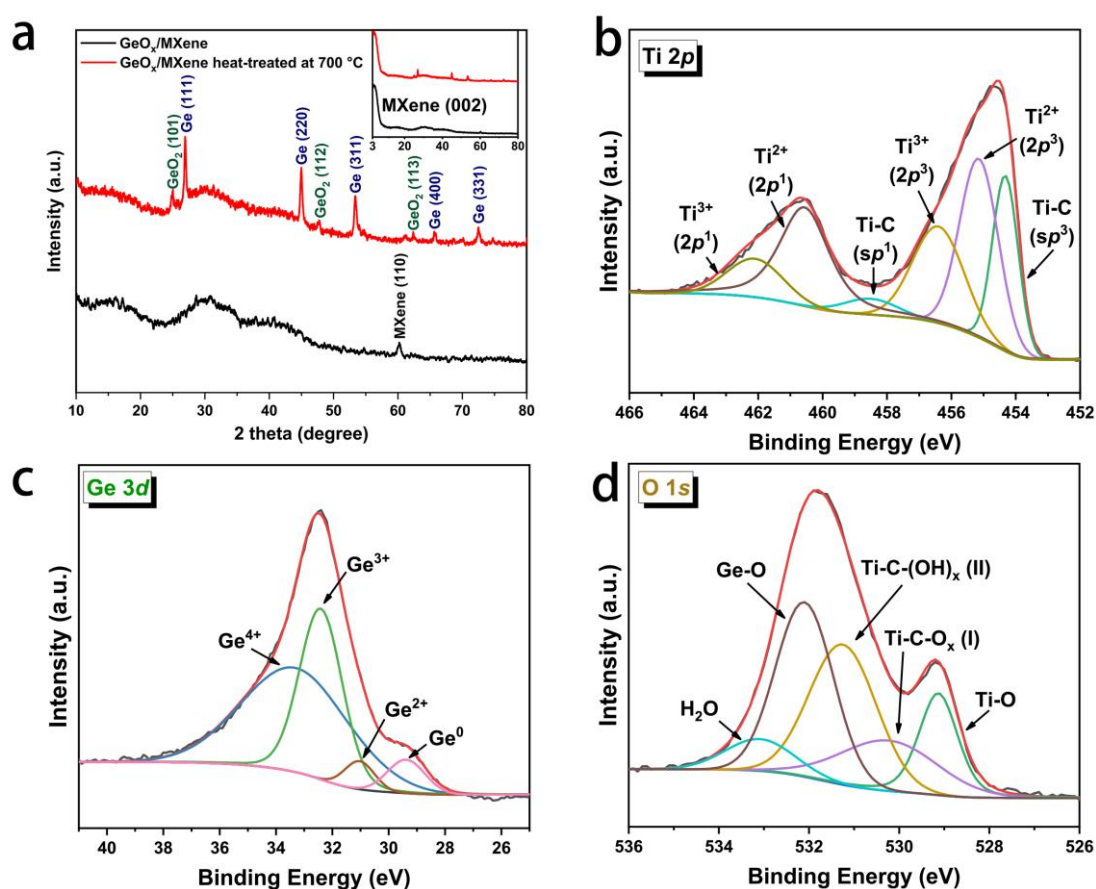


Fig. 3 (a) XRD patterns of $\text{GeO}_x/\text{MXene}$ nanosheets; XPS of (b) Ti 2p, (c) Ge 3d, and (d) O 1s spectrum of the $\text{GeO}_x/\text{MXene}$ nanosheets.

To determine the content of GeO_x in the composite, the weight of the composite (pristine MXene with the reduced GeO_x) was recorded after dried in a vacuum furnace.

The content of GeO_x could be simply calculated by the difference in the weight of

pristine MXene and the GeO_x/MXene composite. To ensure an accurate result, this experiment was repeated several times and the GeO_x content in GeO_x/MXene was calculated to be in the range of 40–43 %. In Fig. S5, the black TG curve of the GeO_x/MXene shows a sharp decrease in weight (38.86%) when the temperatures goes from 700 to 850 °C, which is related to the decomposition of the GeO_x. [22]

Fig. 4 displays the electrochemical performance of the GeO_x/MXene/PVDF (NMP) electrode. The CV curves of GeO_x/MXene/PVDF (NMP) in the voltage range of 0.01 V – 1.2 V with the scan rate of 0.1 mV s⁻¹ were plotted in Fig 4a. For the first lithiation of the GeO_x/MXene, the small current increasing from 1.0 V is related to the formation of SEI between the active materials with the electrolyte. This formation of the SEI layer results in low Coulombic efficiency in the first cycle.[34] With the continuous lithiation, a peak appearing around 0.4 V is associated with the deoxidation of GeO₂. Finally, a sharp peak occurring from 0.3 V to 0.01 V is ascribed to the alloying of Li and Ge to form Li_xGe. In the oxidation curve, the peak at 0.45 V is assigned to the delithiation of Li-Ge alloy.[22] These peaks are also observed in the following cycles, indicating the stable reaction pathway for the lithiation process of GeO_x/MXene composite.

Fig. 4b shows the charge/discharge curves of the GeO_x/MXene/PVDF (NMP) at the current density of 200 mA g⁻¹ in a voltage window from 0.01 V to 1.2 V. [7] A capacity of approximately 2628 mAh g⁻¹ (corresponding to the mass of GeO_x) is maintained in the discharge of the first cycle. By comparison, the pure MXene nanosheet without GeO_x coating exhibits in a capacity of only 35 mA g⁻¹ in the control experiment (Fig.

S6). Therefore, the MXene in the GeO_x/MXene composite only contributed to the capacity of 19 mAh g⁻¹ according to the MXene content (60%). It is clear that a significant drop in capacity for the second and the further cycles. This irreversible capacity loss is probably attributed to the irreversible formation of Li₂O and SEI layers on the GeO_x/MXene nanosheets during the first lithiation. [35, 36] After a few cycles to stabilize the active materials, the shape of the 10th charge-discharge curve is similar to the 30th cycle, revealing good cycling stability of this GeO_x/MXene nanosheets.

The cycling performance of the GeO_x/MXene/PVDF (NMP) and GeO_x/PVDF (NMP) anodes under the current density of 0.2 A g⁻¹ and 0.5 A g⁻¹ is shown in Fig. 4c and 4d. In the cycling performance with the current density of 0.2 A g⁻¹ (Fig. 4c), the GeO_x/MXene/PVDF (NMP) delivers the discharge capacity of 1004 mAh g⁻¹ in the third cycle and retains 826 mAh g⁻¹ after 50 cycles respectively. This result demonstrates good capacity retention in this current density due to the combination of MXene and GeO_x. By comparison, the GeO_x anode alone exhibits a discharge capacity of 648 mAh g⁻¹ in the third cycle and retains 335 mAh g⁻¹ after 50 cycles, the retention (51.7 %) of discharge capacity is much lower than that of the GeO_x/MXene/PVDF (NMP) (82.3 %). This extraordinary performance highlights the importance of the addition of MXene structure. The flexible MXene structure nanosheet can significantly release the accumulated stresses during the lithiation process of GeO_x, eventually enhancing the reaction stability of the active materials. When the current density increase to 0.5 A g⁻¹ (Fig. 4d), GeO_x/MXene/PVDF (NMP) achieves a discharge

capacity of 1011 mAh g⁻¹ in the 5th cycle and retains 483 mAh g⁻¹ after 100 cycles. In contrast, the capacity of GeO_x/PVDF (NMP) exhibits a significant decline at this current density, suggesting that the MXene plays an effective role to improve the electrochemical stability of GeO_x in LIBs.

Fig. 4e shows the rate capability of the GeO_x/MXene/PVDF (NMP) anode under the increasing current densities. The discharge capacities reach 1068, 967, 770, 655, 492, and 372 mAh g⁻¹ at different current densities from 0.2, 1, 3, 5, 10 to 15 A g⁻¹. A stable capacity of 372 mAh g⁻¹ (similar to the theoretical capacity of graphite) is achieved even at 15 A g⁻¹. When the current density returns to 1 A g⁻¹, the specific capacity could recover to 893 mAh g⁻¹, indicating excellent rate capability of this GeO_x/MXene nanosheet structure. Remarkably, the discharge capacity of GeO_x/MXene anode is much larger than that of the pure GeO_x at the same current density. This result is explained by the superior conductivity of the MXene used as the active materials in this structure. Moreover, the ultrathin of the GeO_x layer facilitates a fast pathway for lithiation and delithiation processes. Fig 4f displays the charge/discharge profiles of the GeO_x/MXene with various current densities. With increasing current densities, the level of distinct polarization becomes more pronounced. However, the discharge plateaus from 0.35 to 0.01 V are still visible when the current density increases to a high rate of 15 A·g⁻¹, suggesting that GeO_x/MXene composite offers the stable permeability for Li-ion transfer and excellent electrical conductivity with a wide range of current rates.

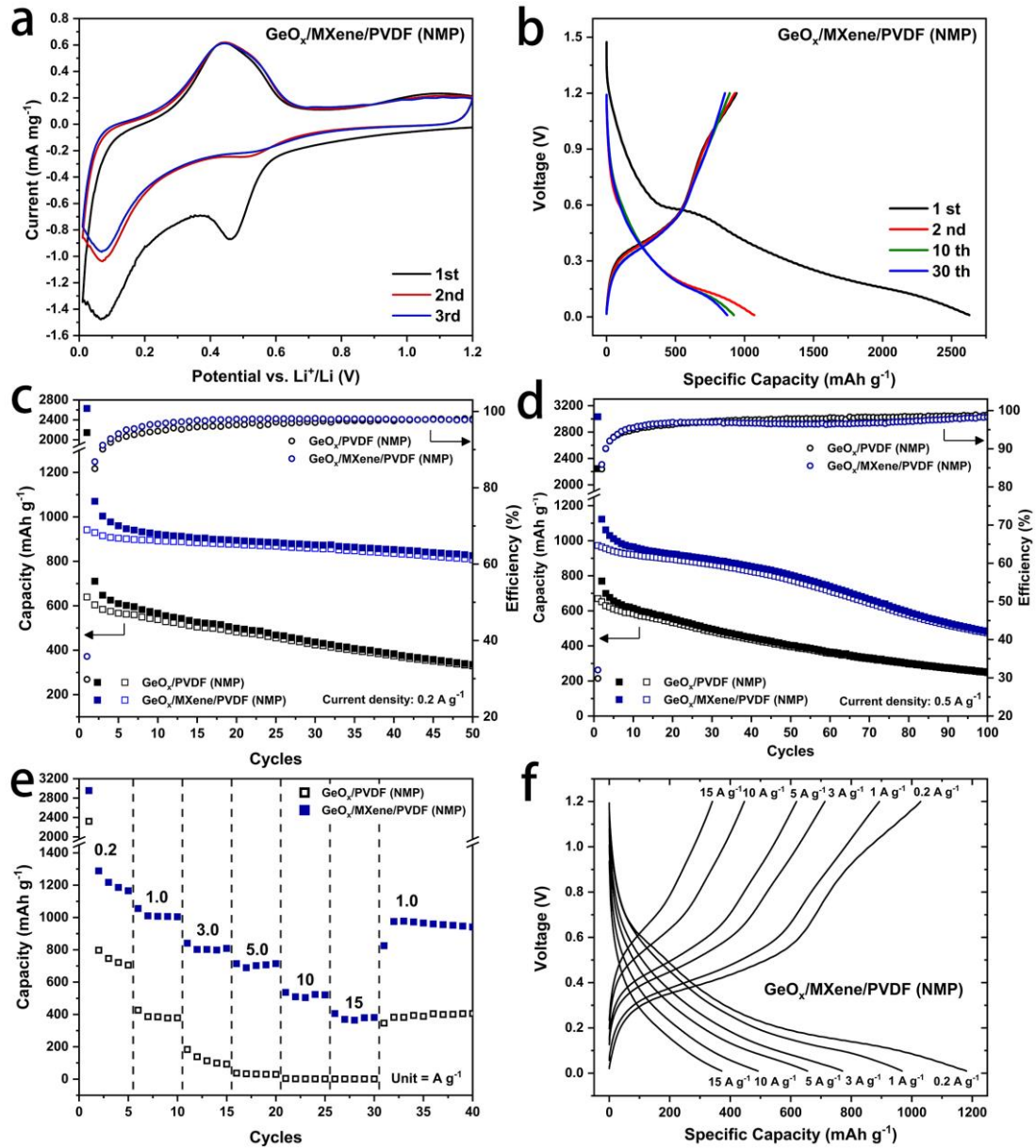


Fig. 4 The Li-ion storage performance of $\text{GeO}_x/\text{MXene}$ anode in LIBs: (a) The CV curves of $\text{GeO}_x/\text{MXene}/\text{PVDF}$ (NMP) between 0.01 V-1.2 V with the scan rate of 0.1 mV s^{-1} ; (b) The galvanostatic charge-discharge curves of the $\text{GeO}_x/\text{MXene}/\text{PVDF}$ (NMP) with current density of 0.2 A g^{-1} ; (c and d) Cycling performance of $\text{GeO}_x/\text{MXene}/\text{PVDF}$ (NMP) and GeO_x/PVDF (NMP) anodes with charge/discharge current density of 0.2 A g^{-1} and 0.5 A g^{-1} ; (e) Rate performance of $\text{GeO}_x/\text{MXene}/\text{PVDF}$ (NMP) and GeO_x/PVDF (NMP) anodes with current densities from 0.2 to 15 A g^{-1} ; (f) Galvanostatic charge-discharge curves of $\text{GeO}_x/\text{MXene}/\text{PVDF}$ (NMP) with current densities from 0.2 to 15 A g^{-1} .

Fig. 5 displays the SEM images of the GeO_x/MXene/PVDF (NMP) electrode before and after 100 cycles at the current density of 0.2 A g⁻¹. Interestingly, as seen in Fig. 5a and 5b, an uneven dispersion and agglomeration of nanosheet are observed for the fresh GeO_x/MXene/PVDF (NMP) electrode, resulting in the porous structure in the electrode. One possible explanation for this effect is that the hydrophilic property of GeO_x/MXene in the hydrophobic NMP solvent tends to be agglomerated. However, this phenomenon does not exist in the pure GeO_x electrode when using NMP or DI-water solvent (Fig. S7), which confirms that the difference in dispersion and porous structure are probably associated with the MXene-based nanosheet structure due to its unique structure and hydrophilic properties.

Fig. 5b and 5c show the cross-section of GeO_x/MXene/PVDF (NMP) electrodes before and after 100 cycles to investigate the mechanical stability of the electrode structure. The pristine electrode of GeO_x/MXene/PVDF (NMP) exhibits a thickness of 25 μm (Fig. 5b). After 100 cycles, the thickness of the GeO_x/MXene/PVDF (NMP) electrode increases to 50.9 μm (Fig. 5c) with a volume expansion of 198.4%. Although the structure of the GeO_x/MXene/PVDF (NMP) electrode demonstrates a satisfying improvement of the stability (Fig. 4d), the volume expansion in LIBs is significant. Nano-size porous structure of electrode materials has been proposed to accommodate the volume expansion [37, 38]. According to the current study, the presence of weak and largely micro-size porous structure in the GeO_x/MXene/PVDF (NMP) plays little role on accommodating the huge stress effect during the lithiation of GeO_x, therefore

the large volume expansion and rapid capacity fading were observed. Clearly, this issue needs to be solved for its wide applications in LIBs.

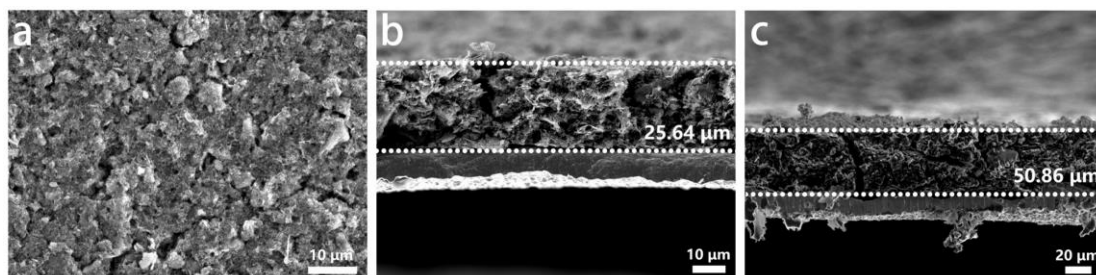


Fig. 5 SEM images of the GeO_x/MXene/PVDF (NMP) electrode. (a) Top-view; (b) Cross-section of fresh electrode; (c) Cross-section after 100 cycles at the current density of 0.2 A g⁻¹.

GeO_x/MXene Anode with Li-PAA Binder and DI-water Solvent

Driven by tackling the large volume expansion that is occurred on the GeO_x/MXene/PVDF (NMP) electrode, we consider another approach to modify the structure of the anode. When the powder-like active materials are used in the electrode, the slurry preparation is a crucial step for the electrochemical performance in LIBs. Commonly, the PVDF binder is selected in the anode preparation [9, 34, 39]. Recently, the Li-PAA has also been considered as a promising binder for the large-volume change alloy materials in electrodes, because it exhibits better elastomeric and mechanical properties than PVDF binder. [40] Therefore, the water-based Li-PAA has been used for slurry preparation for the GeO_x-based materials and already proved outstanding electrochemical performance. [21, 22] However, little efforts have been made to compare the solubility of the solvent used such as water-insoluble PVDF and

water-soluble Li-PAA . Under different solubility of the solvent, the dispersion rate of the active materials could exhibit a distinct state, which eventually affects the final state of the composite. Considering the hydrophilic nature of MXene based nanosheet, it is important to investigate the influence of solvent with hydrophilia properties of the electrode in the LIBs.

Fig. 6 and Fig. S8 display the electrochemical performance of the $\text{GeO}_x/\text{MXene}/\text{Li-PAA}$ (DI-water) electrode. As shown in Fig. S8a, the CV curves of $\text{GeO}_x/\text{MXene}/\text{Li-PAA}$ (DI-water) are similar to the $\text{GeO}_x/\text{MXene}/\text{PVDF}$ (NMP) except for the first lithiation step (Fig. 4a). A large current was observed for the $\text{GeO}_x/\text{MXene}/\text{PVDF}$ (NMP) in the first cycle during the formation of SEI, which directly results from the enlarged contact area between active materials and electrolyte. In fact, it is difficult for hydrophilic materials ($\text{GeO}_x/\text{MXene}$) to disperse in the hydrophobic solvent (PVDF). This reasoning would be further confirmed and discussed in the following discussions. Fig. S8b shows the charge/discharge curves of the $\text{GeO}_x/\text{MXene}/\text{Li-PAA}$ (DI-water), which exhibits the same charge and discharge characteristics as Fig. 4b. Moreover, the capacity (2102 mAh g^{-1}) of the first discharge curve is smaller probably associated with the uniformly coated water-soluble Li-PAA binder, which is supported in the corresponding CV curves as shown in Fig. S8a.

Fig 6a and 6b illustrate the cycling performance of the $\text{GeO}_x/\text{MXene}$ and pure GeO_x anodes with different binders and solvents under the current densities of 0.2 A g^{-1} and

0.5 A g⁻¹. As shown in Fig. 6a, the GeO_x/MXene/Li-PAA (DI-water) delivers a discharge capacity of 1091 mAh g⁻¹ after the first three cycles and retains 1026 mAh g⁻¹ after 50 cycles with the current density of 0.2 A g⁻¹, showing a further enhancement of capacity retention. In the cycling performance with the current density of 0.5 A g⁻¹ (Fig. 6b), the GeO_x/MXene/Li-PAA (DI-water) still achieves excellent cycling stabilization, corresponding to a discharge capacity of 1078 mAh g⁻¹ at 5th cycle and retains 950 mAh g⁻¹ after 100 cycles. By contrast, the capacity of GeO_x/MXene/PVDF (NMP) and GeO_x/Li-PAA (DI-water) exhibits a noticeable decline at this current density (Fig. 6a). Interestingly, GeO_x/MXene anode prepared with Li-PAA binder and DI-water solvent shows the superior electrochemical performance. The hydrophilic nature of GeO_x/MXene nanosheet leads to a uniform dispersion in DI-water, forming a tight crosslink with Li-PAA binder in the electrode and resulting in a significant improvement of the electrochemical stability.

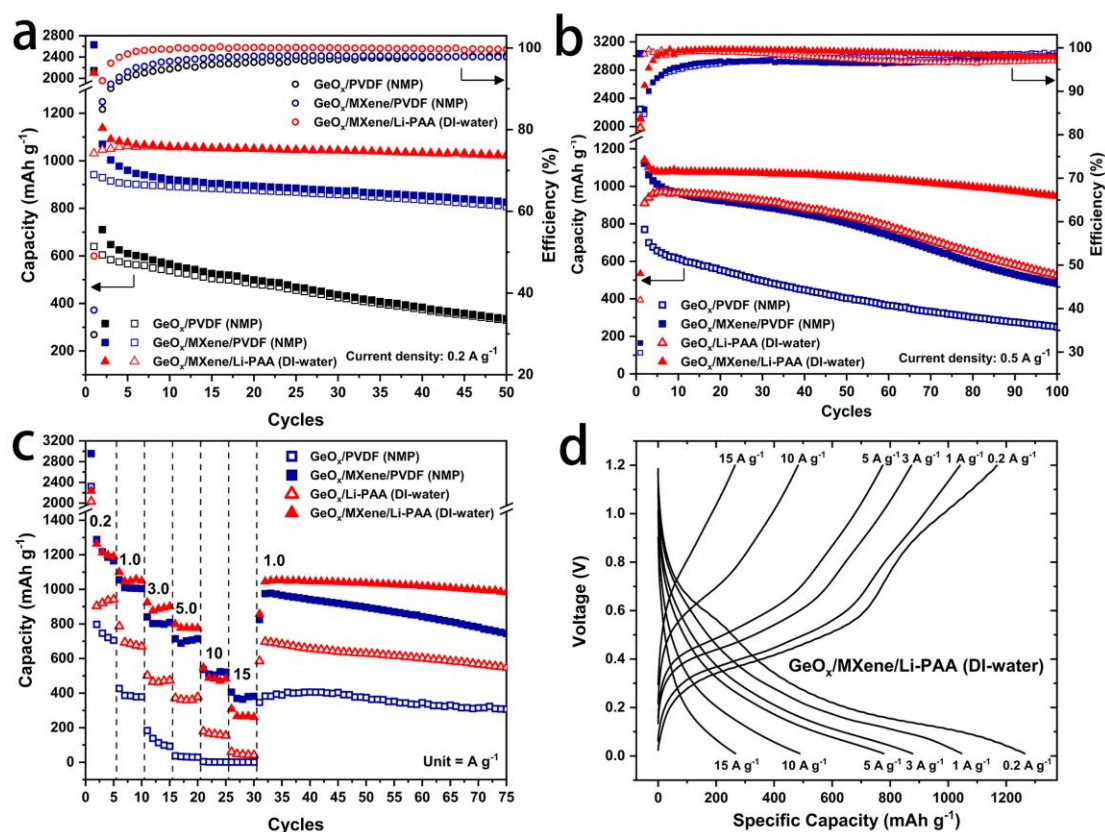


Fig. 6 The Li-ion storage performance of $\text{GeO}_x/\text{MXene}/\text{Li-PAA}$ (DI-water) anode in LIBs: (a and b) Cycling performance of $\text{GeO}_x/\text{MXene}$ and GeO_x anodes with charge/discharge current density of 0.2 A g^{-1} and 0.5 A g^{-1} ; (c) Rate performance of $\text{GeO}_x/\text{MXene}$ with current densities from 0.2 to 15 A g^{-1} ; (d) Galvanostatic charge-discharge curves of $\text{GeO}_x/\text{MXene}/\text{Li-PAA}$ (DI-water) with current densities from 0.2 to 15 A g^{-1} .

The corresponding rate capability (Fig. 6c) of the $\text{GeO}_x/\text{MXene}$ with different binders and solvents is analogous in general to the corresponding cycling performance as seen in Fig. 6a and 6b. The discharge capacities of $\text{GeO}_x/\text{MXene}/\text{Li-PAA}$ (DI-water) reach 1191, 1049, 901, 776, 482, and 261 mAh g^{-1} at different current densities from 0.2, 1, 3, 5, 10 to 15 A g^{-1} . Furthermore, the specific capacity can recover to 1046 mAh g^{-1}

when the current density resets to 1 A g^{-1} , and excellent capacity stability remains in further dozens of cycles. By contrast, for the $\text{GeO}_x/\text{MXene}/\text{PVDF}$ (NMP), the discharge capacities are slightly lower than that of the $\text{GeO}_x/\text{MXene}/\text{Li-PAA}$ (DI-water) in the current densities from 0.2 to 5 A g^{-1} . However, when the current density increases to 10 and 15 A g^{-1} , the rate capabilities are 521 mAh g^{-1} at 10 A g^{-1} and 381 mAh g^{-1} at 15 A g^{-1} , suggesting a better performance than the capacity of $\text{GeO}_x/\text{MXene}/\text{Li-PAA}$ (DI-water). This result was not observed in the pure GeO_x nanoparticle structure for both DI-water and NMP solvent, probably attributed to the unique nanosheet structure and hydrophilic properties of the $\text{GeO}_x/\text{MXene}$ materials. As shown in Fig. 6c, the $\text{GeO}_x/\text{Li-PAA}$ (DI-water) exhibits a larger rate capacity than GeO_x/PVDF (NMP) at the same current density, which is opposite to the results from the $\text{GeO}_x/\text{MXene}$ anode. The better rate performance of the $\text{GeO}_x/\text{Li-PAA}$ (DI-water) anode is probably explained by the good Li^+ conductivity of Li-PAA. [40, 41] The charge/discharge profiles of $\text{GeO}_x/\text{MXene}/\text{Li-PAA}$ (DI-water) with various current densities are plotted in Fig. 6d. Similar pulverization behavior and voltage plateau to $\text{GeO}_x/\text{MXene}/\text{PVDF}$ (NMP) are observed, indicating outstanding permeability and excellent stability of Li-ion in this electrode.

To further understand the electrochemical kinetics of $\text{GeO}_x/\text{MXene}$ anode with different binders and solvents in Li-ion storage, a series of CV curves with various scan rates from 0.1 to 1 mV s^{-1} are illustrated in Fig. 7a and 7d. Typically, the current (i) versus scan rate (ν) should follow the equation (3) and (4) [42]:

$$i = av^b \quad (3)$$

$$\log(i) = b \log(v) + \log(a) \quad (4)$$

In these equations, the value b could be obtained by the slope of $\log(i)$ versus $\log(v)$. b is a useful factor to evaluate the process of diffusion or capacity-controlled procedure. If b is 0.5, the diffusion-controlled process is dominated in the electrochemical storage, while if b is equal to 1, a capacity behavior plays a more important role.

When plotting the $\log(v)$ with scan rate and $\log(i)$ of $\text{GeO}_x/\text{MXene}$ from 0.1 to 1 mV s^{-1} , a linear relationship is observed in Fig. 7b and 7e. For the $\text{GeO}_x/\text{MXene}/\text{PVDF}$ (NMP), the parameter b is calculated as 0.71/0.70 corresponding to reduction/oxidation peaks. The value of b between 0.5 and 1 indicates the synergistic effect of diffusion-controlled and capacitance-controlled behaviors in electrochemical energy storage, which is attributed to the $\text{GeO}_x/\text{MXene}$ nanosheet provides abundant fast pathway for ion diffusion. For $\text{GeO}_x/\text{MXene}/\text{Li-PAA}$ (DI-water), the parameter b is slightly smaller than the above result, corresponding to 0.58/0.60 for reduction/oxidation processes, respectively. The lower parameter b implies a diffusion-controlled behavior. Therefore, the compact structure of the $\text{GeO}_x/\text{MXene}/\text{Li-PAA}$ (DI-water) electrode is not in favor of anchoring of Li-ions on the surface of active materials. The parameter b is probably attributed to the differences in the structure of two electrodes. As shown in Fig. 5, the $\text{GeO}_x/\text{MXene}/\text{PVDF}$ (NMP) exhibits a porous structure, which was formed due to the hydrophilic $\text{GeO}_x/\text{MXene}$ tending to be agglomerated in the hydrophobic NMP solvent.

The porous structure of $\text{GeO}_x/\text{MXene}/\text{PVDF}$ (NMP) composite assisted the Li-ions in

anchoring on the surface of the electrode, and, further improved the rate performance and capacitive-controlled proportion in the electrochemical test. However, with regard to the GeO_x/MXene/Li-PAA (DI-water), the well-distribution of GeO_x/MXene in water solvent forms a compact structure in the electrode. This compact structure slightly reduces the expose area of the electrode with the electrolyte, therefore the smaller parameter *b* was measured from the electrode. However, it is worth noting that the compact and tight structure is beneficial to prevent the pulverization of whole electrode and thus an outstanding cycle stabilization, as shown in Fig. 6. Moreover, the compact structure in the GeO_x/MXene/Li-PAA (DI-water) electrode was confirmed and described in Fig. 8.

The capacitance and diffusion contribution ratios of the GeO_x/MXene could be further quantified by splitting the current response (*i*) to diffusion-controlled insertion ($k_2v^{1/2}$) and capacitive reactions (k_1v) via the following equations [43]

$$i(v) = k_1v + k_2v^{1/2} \quad (5)$$

$$i(v)/v^{1/2} = k_1v^{1/2} + k_2 \quad (6)$$

The constants *k*₁ and *k*₂ could be calculated by plotting $v^{1/2}$ versus $i(v)/v^{1/2}$ with different response currents and the scan rates. Finally, by computing *k*₁ and *k*₂, the contribution ratio of diffusion-controlled insertion ($k_2v^{1/2}$) and capacitive reactions (k_1v) can be determined, as shown in Fig. 7c and 7f. When the sweep rate increases from 0.1 to 1 mV s⁻¹, the capacitive-controlled proportion of the GeO_x/MXene/PVDF (NMP) approaches a maximum value of 65%. By comparison, the capacitive-controlled

proportion for GeO_x/MXene/Li-PAA (DI-water) is around 10% smaller than that of the GeO_x/MXene/PVDF (NMP). This difference further supports the difference of rate capability for two types of electrodes displayed in Fig. 6c.

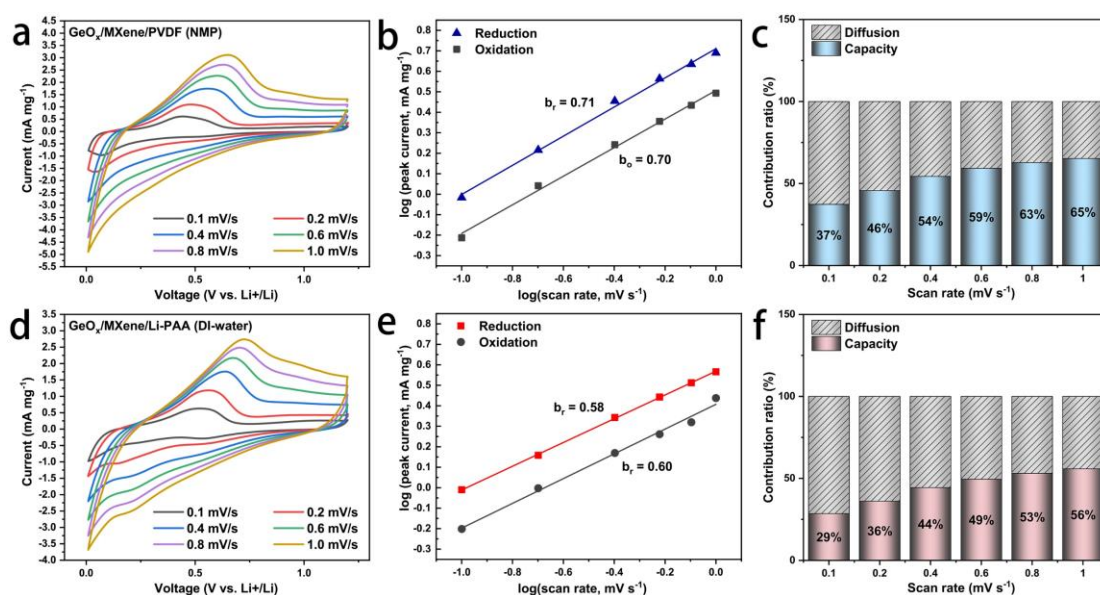


Fig. 7 The CV curves of the (a) GeO_x/MXene/PVDF (NMP) and (d) GeO_x/MXene/Li-PAA (DI-water) with different scan rates from 0.1 to 1 mV s⁻¹; the log(*v*) versus log(*i*) curves and determined b-values based on the reduction peaks for (b) GeO_x/MXene/PVDF (NMP) and (e) GeO_x/MXene/Li-PAA (DI-water); The contribution of diffusion-controlled and capacitive-controlled capacities for (c) GeO_x/MXene/PVDF (NMP) and (f) GeO_x/MXene/Li-PAA (DI-water) at various scan rates from 0.1 to 1 mV s⁻¹.

The fact that different electrode structures are directly associated with the improved cycling stability of GeO_x/MXene anode using different binders and solvents in LIBs. As shown in Fig. 8a and 8b, GeO_x/MXene/Li-PAA (DI-water) electrode exhibits

smooth and compact structure in electrode, obviously very different from the observed GeO_x/MXene/PVDF (NMP) electrode structure (Fig. 5a and 5b). Fig. 8b and 8c show the cross-section SEM images of GeO_x/MXene/Li-PAA (DI-water) before and after 100 cycles. As marked in the images, the electrode retains a similar thickness before cycling (20.2 μm) and after 100 cycles (22.5 μm). Compared with the GeO_x/MXene/PVDF (NMP) electrode as seen in Fig. 5b and 5c, the GeO_x/MXene/Li-PAA (DI-water) electrode have demonstrated an effective alleviation of volume expansion of the GeO_x. One possible explanation is that the well-distributed and compact structure could effectively restrict the volume change of GeO_x materials. Here a proposed structural mechanism of these two types of electrodes is described in Fig. 9. The resulting excellent rate performance of GeO_x/MXene anode is ascribed to the uniform growth of the GeO_x nanoparticles on the MXene nanosheet, which provides a fast pathway for both electron and ion during lithiation and delithiation processes. However, the GeO_x/MXene nanosheets display different features when the electrode is prepared with different combinations of binders and solvents. The hydrophobic PVDF (NMP) solvent makes the electrode aggregated and difficult to disperse. The consequence of that is to create more pores to allow the Li-ions passing through the electrode when interacting with the active materials. But this porous structure is probably too weak to mediate the huge stress effect during the lithiation of GeO_x. Contrarily, the electrode prepared with Li-PAA (DI-water) has a more compact and tight structure, offering a good ability to prevent the pulverization of the whole electrode and demonstrating an excellent cycle stabilization. However, this compact structure on the other hand blocks the active sites

and limits the free shuttle of the Li-ions, contributing a slight decrease in rate performance (Fig. 6c). Overall, the GeO_x/MXene/Li-PAA (DI-water) electrode demonstrates an effective strategy to inhibit the pulverization of the GeO_x materials, in the other words, the combination of Li-PAA binder and DI-water solvent is more suitable for the composition of alloyed anodes materials with MXene nanosheet in LIBs. However, the combination of PVDF binder and NMP solvent seems a better choice for other materials which does not suffer the huge volume change during the lithiation, since it could provide more active sites and fast pathway for Li-ions, leading to improved electrochemical kinetics and rate capability in the electrochemical properties.

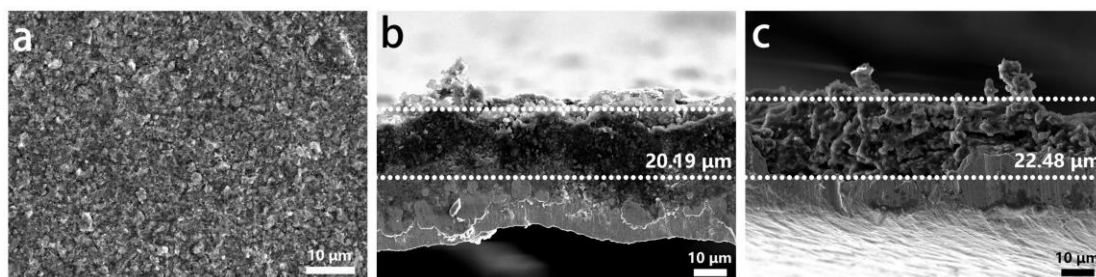


Fig. 8 SEM images of the GeO_x/MXene/Li-PAA (DI-water) electrode. (a) Top-view; (b) Cross-section of fresh electrode; (c) Cross-section after 100 cycles at the current density of 0.2 A g⁻¹.

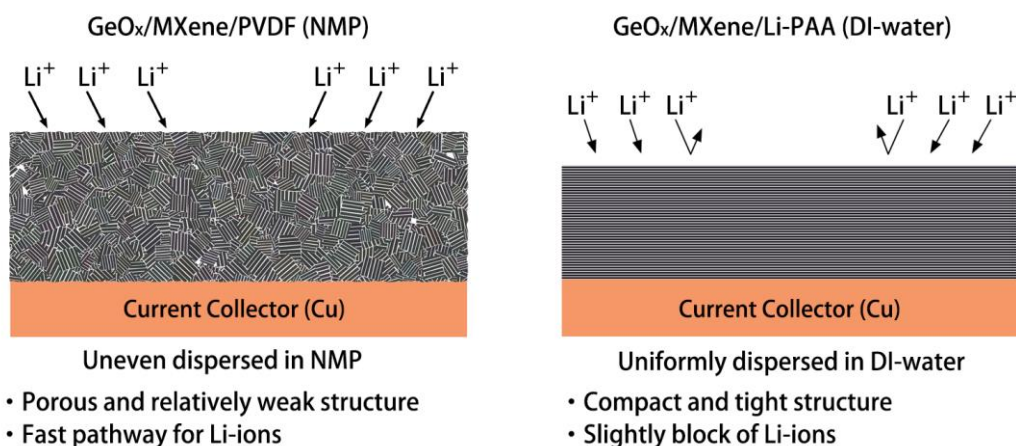


Fig. 9 Structural schematics of GeO_x/MXene/PVDF (NMP) and GeO_x/MXene/Li-PAA (DI-water)

Conclusion

In this study, we have demonstrated a facile one-pot approach to fabricate the GeO_x/MXene nanosheet composite, where the amorphous GeO_x nanoparticles were uniformly coated on the MXene nanosheets. This MXene nanosheet and GeO_x nanoparticles significantly enhance the electrical conductivity and Li-ion interaction kinetics in the LIBs. In addition, interesting results are found when GeO_x/MXene electrodes prepared by two different slurries with different combinations of binders and solvents, offering alternative enhancement in the electrochemical properties. For GeO_x/MXene/PVDF (NMP), the electrode exhibits an excellent sustainable capacity of 381 mAh g⁻¹ at 15 A g⁻¹. By contrast, the GeO_x/MXene/Li-PAA (DI-water) electrode demonstrates a reversible capacity of 950 mAh g⁻¹ at 0.5 A g⁻¹ after 100 cycles. These differences were further analyzed by the structure and the contribution of diffusion-controlled and capacitive-controlled capacities of these electrodes. The SEM results reveal the presence of porous structure in the GeO_x/MXene/PVDF (NMP) due to the

uneven dispersion of the GeO_x/MXene nanosheet in the electrode. This porous structure could provide more pathway for Li-ions, but reduce the mechanical strength of the whole electrode. For the GeO_x/MXene/Li-PAA (DI-water) electrode, a compact and tight structure is observed, which offers a robust mechanical strength for the whole electrode. However, this tight structure might block the channel of Li-ions, leading to relatively lower electrochemical kinetics and rate capability. This work not only proposes a simple method to synthesize the GeO_x-based and 2D MXene composite materials for high-performance LIBs but also provides new insights for tuning the electrochemical properties through the choice of binder and solvent.

Acknowledgments

This work was supported by the National Natural Science Foundation of China (NSFC Grants 21750110441), State Key Laboratory of Materials Processing and Die & Mould Technology, Huazhong University of Science and Technology (P2019-019), Suzhou Industrial Park Initiative Platform Development for Suzhou Municipal Key Lab for New Energy Technology (RR0140), and Key Program Special Fund in XJTLU (KSF-A-04, KSF-E-28, KSF-E-38).

Reference

- [1] M. Armand, J.M. Tarascon, Building Better Batteries, *Nature*, 451 (2008) 652-657.
- [2] J.M. Tarascon, M. Armand, Issues and Challenges Facing Rechargeable Lithium Batteries, *Nature*, 414 (2001) 359-367.
- [3] J.B. Goodenough, K.S. Park, The Li-ion Rechargeable Battery: a Perspective, *J. Am. Chem. Soc.*, 135 (2013) 1167-1176.
- [4] V. Etacheri, R. Marom, R. Elazari, G. Salitra, D. Aurbach, Challenges in the Development of Advanced Li-ion Batteries: A Review, *Energy Environ. Sci.*, 4 (2011).
- [5] Y.P. Wu, E. Rahm, R. Holze, Carbon Anode Materials for lithium Ion Batteries, *J. Power Sources*, 114 (2003) 228-236.
- [6] S. Wu, C. Han, J. Iocozzia, M. Lu, R. Ge, R. Xu, Z. Lin, Germanium-Based Nanomaterials for Rechargeable Batteries, *Angew. Chem. Int. Ed.*, 55 (2016) 7898-7922.
- [7] S. Jin, N. Li, H. Cui, C. Wang, Growth of the Vertically Aligned Graphene@amorphous GeO(x) Sandwich Nanoflakes and Excellent Li Storage Properties, *Nano Energy*, 2 (2013) 1128-1136.
- [8] C.K. Chan, X.F. Zhang, Y. Cui, High Capacity Li-ion Battery Anodes Using Ge Nanowires, *Nano Lett.*, 8 (2008) 307-309.
- [9] S. Yan, H. Song, S. Lin, H. Wu, Y. Shi, J. Yao, GeO(2) Encapsulated Ge Nanostructure with Enhanced Lithium-Storage Properties, *Adv. Funct. Mater.*, 29 (2019).
- [10] S. Wu, R. Wang, Z. Wang, Z. Lin, CuGeO(3) Nanowires Covered with Graphene

as Anode Materials of Lithium Ion Batteries with Enhanced Reversible Capacity and Cyclic Performance, *Nanoscale*, 6 (2014) 8350-8358.

[11] Q. Liu, Y. Zhou, J. Kou, X. Chen, Z. Tian, J. Gao, S. Yan, Z. Zou, High-yield Synthesis of Ultralong and Ultrathin Zn(2)GeO(4) Nanoribbons Toward Improved Photocatalytic Reduction of CO(2) into Renewable Hydrocarbon Fuel, *J. Am. Chem. Soc.*, 132 (2010) 14385-14387.

[12] F. Jia, L. Song, W. Wei, P. Qu, M. Xu, Facile One-pot Method Synthesis CNT-GeO(2) Nanocomposite for High Performance Li-ion Battery Anode Material, *New J. Chem.*, 39 (2015) 689-695.

[13] J. Zhang, T. Yu, J. Chen, H. Liu, D. Su, Z. Tang, J. Xie, L. Chen, A. Yuan, Q. Kong, Germanium-based Complex Derived Porous GeO(2) Nanoparticles for Building High Performance Li-ion Batteries, *Ceram. Int.*, 44 (2018) 1127-1133.

[14] J. Wu, N. Luo, S. Huang, W. Yang, M. Wei, Reversible Conversion Reaction of GeO(2) Boosts Lithium-ion Storage via Fe Doping, *J. Mater. Chem. A*, 7 (2019) 4574-4580.

[15] X. Liu, J. Zai, B. Li, J. Zou, Z. Ma, X. Qian, Na(2)Ge(4)O(9) Nanoparticles Encapsulated in 3D Carbon Networks with Long-term Stability and Superior Rate Capability in Lithium Ion Batteries, *J. Mater. Chem. A*, 4 (2016) 10552-10557.

[16] G. Gao, Y. Xiang, S. Lu, B. Dong, S. Chen, L. Shi, Y. Wang, H. Wu, Z. Li, A. Abdelkader, K. Xi, S. Ding, CTAB-assisted Growth of Self-supported Zn(2)GeO(4) Nanosheet Network on a Conductive Foam as a Binder-free Electrode for Long-life Lithium-ion Batteries, *Nanoscale*, 10 (2018) 921-929.

- [17] S. Jin, G. Yang, H. Song, H. Cui, C. Wang, Ultrathin Hexagonal 2D Co(2)GeO(4) Nanosheets: Excellent Li-Storage Performance and ex Situ Investigation of Electrochemical Mechanism, *ACS Appl. Mater. Interfaces*, 7 (2015) 24932-24943.
- [18] W. Wei, A. Tian, F. Jia, K. Wang, P. Qu, M. Xu, Green Synthesis of GeO(2)/graphene Composites as Anode Material for Lithium-ion Batteries with High Capacity, *RSC Adv.*, 6 (2016) 87440-87445.
- [19] Z. Chen, Y. Yan, S. Xin, W. Li, J. Qu, Y.-G. Guo, W.-G. Song, Copper Germanate Nanowire/Reduced Graphene Oxide Anode Materials for High Energy Lithium-ion Batteries, *J. Mater. Chem. A*, 1 (2013).
- [20] H. Qiu, L. Zeng, T. Lan, X. Ding, M. Wei, In-situ Synthesis of GeO(2)/reduced Graphene Oxide Composite on Ni Foam Substrate as a Binder-free Anode for High-capacity Lithium-ion Batteries, *J. Mater. Chem. A*, 3 (2015) 1619-1623.
- [21] X.L. Wang, W.Q. Han, H. Chen, J. Bai, T.A. Tyson, X.Q. Yu, X.J. Wang, X.Q. Yang, Amorphous Hierarchical Porous GeO(x) as High-capacity Anodes for Li-ion Batteries with Very Long Cycling Life, *J. Am. Chem. Soc.*, 133 (2011) 20692-20695.
- [22] D. Lv, M.L. Gordin, R. Yi, T. Xu, J. Song, Y.-B. Jiang, D. Choi, D. Wang, GeO(x)/Reduced Graphene Oxide Composite as an Anode for Li-Ion Batteries: Enhanced Capacity via Reversible Utilization of Li(2)O along with Improved Rate Performance, *Adv. Funct. Mater.*, 24 (2014) 1059-1066.
- [23] S.H. Choi, K.Y. Jung, Y.C. Kang, Amorphous GeO(x)-Coated Reduced Graphene Oxide Balls with Sandwich Structure for Long-Life Lithium-Ion Batteries, *ACS Appl. Mater. Interfaces*, 7 (2015) 13952-13959.

- [24] M. Ghidui, M.R. Lukatskaya, M.Q. Zhao, Y. Gogotsi, M.W. Barsoum, Conductive Two-Dimensional Titanium Carbide 'clay' With High Volumetric Capacitance, *Nature*, 516 (2014) 78-81.
- [25] Y.T. Liu, P. Zhang, N. Sun, B. Anasori, Q.Z. Zhu, H. Liu, Y. Gogotsi, B. Xu, Self-Assembly of Transition Metal Oxide Nanostructures on MXene Nanosheets for Fast and Stable Lithium Storage, *Adv. Mater.*, 30 (2018) e1707334.
- [26] M. Naguib, M. Kurtoglu, V. Presser, J. Lu, J. Niu, M. Heon, L. Hultman, Y. Gogotsi, M.W. Barsoum, Two-dimensional Nanocrystals Produced by Exfoliation of Ti_3AlC_2 , *Adv. Mater.*, 23 (2011) 4248-4253.
- [27] S. Kajiyama, L. Szabova, H. Iinuma, A. Sugahara, K. Gotoh, K. Sodeyama, Y. Tateyama, M. Okubo, A. Yamada, Enhanced Li-Ion Accessibility in MXene Titanium Carbide by Steric Chloride Termination, *Adv. Energy Mater.*, 7 (2017).
- [28] X. Tang, X. Guo, W. Wu, G. Wang, 2D Metal Carbides and Nitrides (MXenes) as High-Performance Electrode Materials for Lithium-Based Batteries, *Adv. Energy Mater.*, 8 (2018).
- [29] N. Sun, B.-y. Yang, J.-c. Zheng, Z.-j. He, H. Tong, L.-b. Tang, C.-s. An, B. Xiao, Effect of Synthesis Temperature on the Phase Structure, Morphology and Electrochemical Performance of Ti_3C_2 as an Anode Material for Li-ion Batteries, *Ceram. Int.*, 44 (2018) 16214-16218.
- [30] Y. Zhang, Z. Mu, J. Lai, Y. Chao, Y. Yang, P. Zhou, Y. Li, W. Yang, Z. Xia, S. Guo, MXene/Si@SiO(x)@C Layer-by-Layer Superstructure with Autoadjustable Function for Superior Stable Lithium Storage, *ACS Nano*, 13 (2019) 2167-2175.

- [31] Z. Xiao, Z. Li, P. Li, X. Meng, R. Wang, Ultrafine Ti₃C₂ MXene Nanodots-Interspersed Nanosheet for High-Energy-Density Lithium-Sulfur Batteries, *ACS Nano*, 13 (2019) 3608-3617.
- [32] M.Q. Zhao, C.E. Ren, Z. Ling, M.R. Lukatskaya, C. Zhang, K.L. Van Aken, M.W. Barsoum, Y. Gogotsi, Flexible MXene/carbon Nanotube Composite Paper with High Volumetric Capacitance, *Adv. Mater.*, 27 (2015) 339-345.
- [33] C.E. Ren, M.-Q. Zhao, T. Makaryan, J. Halim, M. Boota, S. Kota, B. Anasori, M.W. Barsoum, Y. Gogotsi, Porous Two-Dimensional Transition Metal Carbide (MXene) Flakes for High-Performance Li-Ion Storage, *ChemElectroChem*, 3 (2016) 689-693.
- [34] N. Sun, C.-l. Peng, J.-c. Zheng, Z.-j. He, H. Tong, L.-b. Tang, C.-s. An, B. Xiao, Self-assembled 3D Network GeO(x)/CNTs Nanocomposite as Anode Material for Li-ion Battery, *Powder Technol.*, 338 (2018) 211-219.
- [35] H. Jia, R. Kloepsch, X. He, J.P. Badillo, M. Winter, T. Placke, One-step Synthesis of Novel Mesoporous Three-dimensional GeO₂ and Its Lithium Storage Properties, *J. Mater. Chem. A*, 2 (2014) 17545-17550.
- [36] J.s.S. Peña, I. Sandu, O. Joubert, F.S.n. Pascual, C.O. Areán, T. Brousse, Electrochemical Reaction Between Lithium and β -Quartz GeO₂, *Electrochem. Solid-State Lett.*, 7 (2004).
- [37] R. Mo, D. Rooney, K. Sun, H.Y. Yang, 3D Nitrogen-doped Graphene Foam with Encapsulated Germanium/nitrogen-doped Graphene Yolk-shell Nanoarchitecture for High-performance Flexible Li-ion Battery, *Nat. Commun.*, 8 (2017) 13949.
- [38] D.T. Ngo, H.T.T. Le, C. Kim, J.-Y. Lee, J.G. Fisher, I.-D. Kim, C.-J. Park, Mass-

- scalable Synthesis of 3D Porous Germanium–carbon Composite Particles as an Ultra-high Rate Anode for Lithium Ion Batteries, *Energy Environ. Sci.*, 8 (2015) 3577-3588.
- [39] Y. Xu, X. Zhu, X. Zhou, X. Liu, Y. Liu, Z. Dai, J. Bao, Ge Nanoparticles Encapsulated in Nitrogen-Doped Reduced Graphene Oxide as an Advanced Anode Material for Lithium-Ion Batteries, *J. Phys. Chem. C*, 118 (2014) 28502-28508.
- [40] J. Li, D.-B. Le, P.P. Ferguson, J.R. Dahn, Lithium Polyacrylate as a Binder for Tin–cobalt–carbon Negative Electrodes in Lithium-ion Batteries, *Electrochim. Acta*, 55 (2010) 2991-2995.
- [41] S. Komaba, K. Okushi, T. Ozeki, H. Yui, Y. Katayama, T. Miura, T. Saito, H. Groult, Polyacrylate Modifier for Graphite Anode of Lithium-Ion Batteries, *Electrochem. Solid-State Lett.*, 12 (2009).
- [42] X. Zhao, H. Xu, Z. Hui, Y. Sun, C. Yu, J. Xue, R. Zhou, L. Wang, H. Dai, Y. Zhao, J. Yang, J. Zhou, Q. Chen, G. Sun, W. Huang, Electrostatically Assembling 2D Nanosheets of MXene and MOF-Derivatives into 3D Hollow Frameworks for Enhanced Lithium Storage, *Small*, (2019) e1904255.
- [43] H. Li, J. Lang, S. Lei, J. Chen, K. Wang, L. Liu, T. Zhang, W. Liu, X. Yan, A High-Performance Sodium-Ion Hybrid Capacitor Constructed by Metal-Organic Framework-Derived Anode and Cathode Materials, *Adv. Funct. Mater.*, 28 (2018).